Efficient Green Emission from Wurtzite Al$_x$In$_{1-x}$P Nanowires

L. Gagliano,[*,†] M. Kruijsse,[†] J. D. D. Schefold,[‡] A. Belabbes,[§] M. A. Verheijen,[†,‖] S. Meuret,[‡] S. Koelling,[†] A. Polman,[‡] F. Bechstedt,[§] J.E.M. Haverkort,[†] and E.P.A.M. Bakkers[†,⊥]

[†]Department of Applied Physics, Eindhoven University of Technology, 5600 MB Eindhoven, The Netherlands

[‡]Center for Nanophotonics, AMOLF, Science Park 104, 1098 XG Amsterdam, The Netherlands

[§]Institut für Festkörpertheorie und -optik, Friedrich-Schiller-Universität, Max-Wien-Platz 1, D-07743 Jena, Germany

[‖]Philips Innovation Laboratories Eindhoven, High Tech Campus 11, 5656AE Eindhoven, The Netherlands

[⊥]Kavli Institute of Nanoscience, Delft University of Technology, 2600 GA Delft, The Netherlands

S *Supporting Information*

ABSTRACT: Direct band gap III–V semiconductors, emitting efficiently in the amber–green region of the visible spectrum, are still missing, causing loss in efficiency in light emitting diodes operating in this region, a phenomenon known as the "green gap". Novel geometries and crystal symmetries however show strong promise in overcoming this limit. Here we develop a novel material system, consisting of wurtzite Al$_x$In$_{1-x}$P nanowires, which is predicted to have a direct band gap in the green region. The nanowires are grown with selective area metalorganic vapor phase epitaxy and show wurtzite crystal purity from transmission electron microscopy. We show strong light emission at room temperature between the near-infrared 875 nm (1.42 eV) and the "pure green" 555 nm (2.23 eV). We investigate the band structure of wurtzite Al$_x$In$_{1-x}$P using time-resolved and temperature-dependent photoluminescence

measurements and compare the experimental results with density functional theory simulations, obtaining excellent agreement. Our work paves the way for high-efficiency green light emitting diodes based on wurtzite III-phosphide nanowires.

KEYWORDS: *Semiconductor nanowire, aluminum indium phosphide, wurtzite, solid state lighting, direct band gap, green*
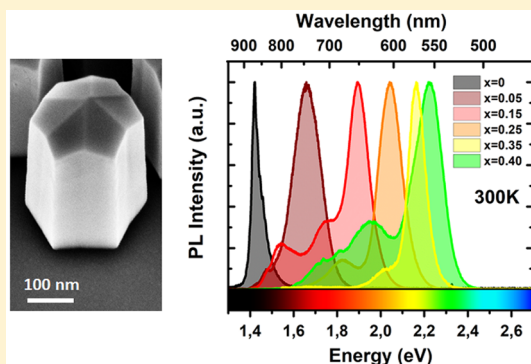
Solid state lighting is widely recognized as the future dominant lighting system, with light emitting diodes (LEDs) play a central role due to their high efficiency, strong brightness, and long operating lifetime over a wide spectrum.[1,2] However, LEDs suffer from fundamental limits such as the efficiency droop at high operating current[3] and, very importantly, low efficiency in the important amber–yellow–green region of the visible spectrum, known as the "green gap".[4,5] This last limit is due to the lack of suitable emitting materials with a direct band gap in the green region.[6,7] Inefficiency in the green–amber region also causes a lack of semiconductor lasers at these wavelengths, where innovative solutions are needed.[8] Semiconductor nanowires have risen as a very promising platform for LEDs[9] and lasers[10] due to their unique properties such as efficient light outcoupling,[11] large junction area,[12] and the possibility to tune their crystal symmetry,[13] opening a new degree of freedom in band structure engineering.[14,15] Recently, wurtzite (WZ) III-phosphide nanowires have been shown to be promising candidates for light emission and lasing, offering a potential route to direct green emission.[16−18]

In this work we achieve the catalyst-free growth of WZ Al$_x$In$_{1-x}$P nanowires with high crystal quality on a (111)A InP substrate, demonstrating direct band gap room-temperature light emission from the infrared range at 875 nm (1.42 eV) to

the green range at 555 nm (2.23 eV). We compare our experimental photoluminescence data with density functional theory calculations to provide a fundamental understanding of the band structure of the WZ Al$_x$In$_{1-x}$P alloy.

The nanowires are grown with selective area metalorganic vapor phase epitaxy (SA-MOVPE) on a (111)A InP substrate with a 50 nm silicon nitride (SiN$_x$) mask. Holes of 150 nm in diameter were fabricated in the SiN$_x$ layer with nanoimprint lithography, forming a square matrix with 512 nm pitch. The growth of WZ Al$_x$In$_{1-x}$P is performed at 700 °C (except for WZ InP, at 750 °C), using trimethylaluminum (TMAl), trimethylindium (TMIn), and phosphine (PH$_3$) as precursors. For the complete growth protocol, see section S1 in the Supporting Information. The V/III ratio during SA-MOVPE growth has been optimized to avoid parasitic growth on the SiN$_x$ layer, to obtain uniform nanowire growth morphology, and to realize wires with high WZ crystal purity. The optimum V/III ratio decreases with increasing Al fraction, reaching a very low value of 3.5 when growing WZ Al$_{0.40}$In$_{0.60}$P. The V/III ratio

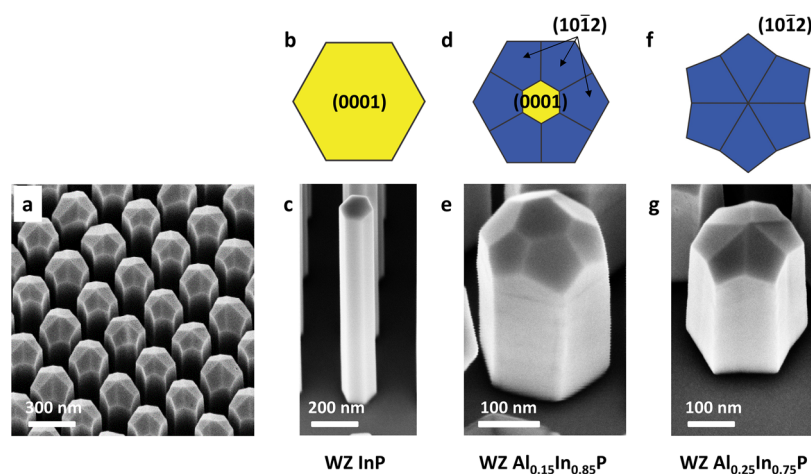**Figure 1.** (a) SEM image of a WZ $Al_{0.25}In_{0.75}P$ nanowire array, showing morphological uniformity of the nanowires. (b−g) SEM images of a WZ $Al_xIn_{1−x}P$ nanowire and schematic drawing of their top faceting. The facets on the top belong to the $\{0001\}$ and $\{10−12\}$ family. (b, c) WZ InP nanowire. (d, e) WZ $Al_{0.15}In_{0.85}P$ nanowire. (f, g) WZ $Al_{0.25}In_{0.75}P$ nanowire.
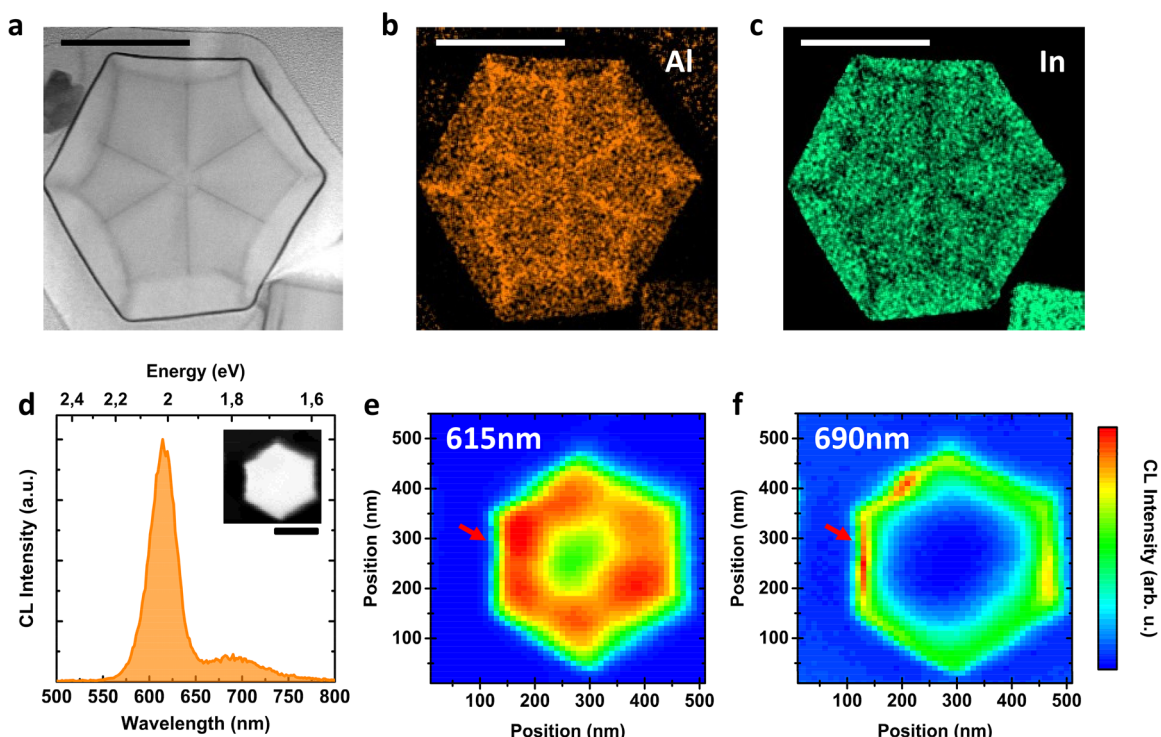

Figure 2. (a−c) Cross-sectional lamella of a WZ $Al_{0.25}In_{0.75}P$ nanowire (average composition). Scale bars: 200 nm. (a) Scanning TEM (STEM) HAADF image. EDS maps of (b) aluminum and (c) indium. (d) Cathodoluminescence spectrum of a WZ $Al_{0.25}In_{0.75}P$ nanowire standing on the substrate, collected with an electron beam oriented parallel to the nanowire axis, aimed at the shell of the nanowire. Two peaks are observed: one at 615 nm (2.05 eV) and one around 690 nm (1.8 eV). Inset: SEM image of the nanowire. Scale bar: 200 nm. Two-dimensional maps of the integrated cathodoluminescence intensity of (e) the 615 nm peak and (f) 690 nm peak integrated over a 50 nm bandwidth. While the 615 nm peak is observed only when aiming toward the core of the nanowire, the 690 nm peak is present only when aiming at the outer region, where we observed the aluminum-poor shell in the EDS analysis. Red arrows: position where the spectrum in part d was collected.

is found to be a critical parameter to obtain WZ crystal purity (see section S1 in the Supporting Information).

The morphology of the nanowires is studied in detail in Figure 1. In Figure 1a we show a representative SEM image of a WZ $Al_xIn_{1−x}P$ nanowire array, in this case WZ $Al_{0.25}In_{0.75}P$, presenting morphological uniformity throughout the sample. WZ $Al_xIn_{1−x}P$ nanowires with $x > 0$ feature a lower aspect ratio than WZ InP, as shown in the SEM images in Figure 1c,e,g. In Figure 1b,d,f we schematically illustrate the corresponding top

faceting of the nanowires in Figure 1c,e,g. While WZ InP always presents a single (0001) top facet, WZ $Al_xIn_{1−x}P$ shows 6 $\{10−12\}$ facets. The presence of complex faceting has been documented in wurtzite nanowires such as GaN[19,20] and ZnO[21] and is commonly explained by the kinetic stability of the slowest growing facets. All WZ $Al_xIn_{1−x}P$ with $x \geq 0.25$ in fact presented a dodecagonal cross section as shown in Figure 1f,g, instead of the typical hexagonal one of WZ InP. We therefore conclude that the change in precursor composition and V/III
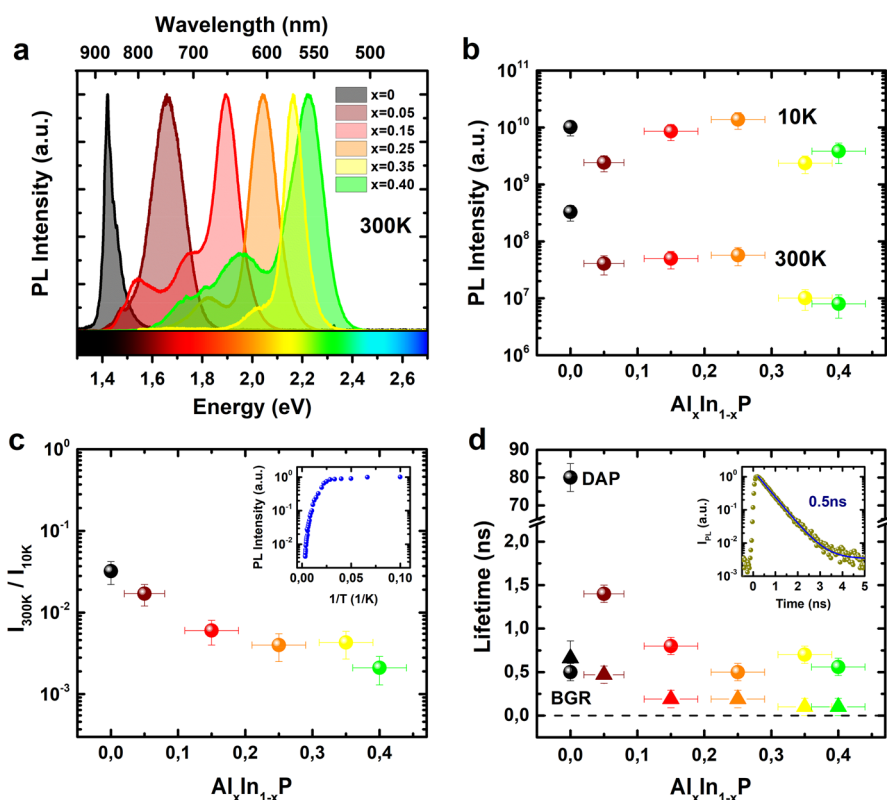
Figure 3. (a) Normalized photoluminescence emission at 300 K of several WZ $Al_xIn_{1-x}P$ nanowire arrays, emitting between 875 nm (1.42 eV) and 555 nm (2.23 eV) in the green range. (b) Integrated PL intensity at 10 and 300 K. (c) Ratio between integrated PL at 300 and 10 K (I_{300K}/I_{10K}), measured at excitation power 1 kW/cm². Inset: integrated photoluminescence as a function of the inverse of temperature of the WZ $Al_{0.25}In_{0.75}P$ nanowire array. (d) Carrier lifetime of the WZ $Al_xIn_{1-x}P$ nanowire arrays at 10 K (circles) and 300 K (triangles). Two lifetimes are reported for WZ InP at 10 K, band-gap-related (BGR) and donor–acceptor pair (DAP) recombination. WZ $Al_xIn_{1-x}P$ with $x > 0$ showed short lifetime, compatible with direct band gap emission. Inset: TRPL decay curve of the WZ $Al_{0.25}In_{0.75}P$ nanowire array at 10 K, fitted by a single exponential decay curve, with 0.5 ns carrier lifetime. Excitation pulse: 1 μJ/cm², corresponding to an average excitation power of 50 W/cm².

ratio affected the ratio between the growth rate of the different families of side facets from the {0001} of WZ InP to the {10−12} of WZ $Al_xIn_{1-x}P$.

The crystal structure and the chemical composition of the WZ $Al_xIn_{1-x}P$ nanowires are investigated with transmission electron microscopy (TEM) for all compositions in this study. The crystal phase of the nanowires with $x < 0.25$ is WZ with stacking faults (up to about 50 sf/μm), while for $x \geq 0.25$ we find WZ with a very low (<1 sf/μm) stacking fault density, suggesting that Al promotes the formation of the WZ phase (see section S2 in the Supporting Information for details). Energy-dispersive X-ray spectroscopy (EDS) is used to quantify the atomic composition. To gain insight on the inner structure of the nanowires, we performed a cross-sectional TEM study on a nanowire cut in a 100 nm thick lamella by focused ion beam (FIB) perpendicularly to the growth axis, as shown in Figure 2a−c. Here, a complex structure is observed. Al-rich segregations ($x = 0.35 \pm 0.03$) with a 6-fold symmetry are observed, which radially connect to an Al-rich $Al_xIn_{1-x}P$ inner shell. The whole structure is surrounded by a shell with lower Al concentration ($x = 0.20 \pm 0.03$) compared to the regions in the core ($x = 0.25 \pm 0.03$). Such segregations with 6-fold symmetry starting from the corners of the core nanowire have been reported before for zincblende (ZB) $Al_xIn_{1-x}P$,[22] AlGaAs,[23] and other core–shell[9,18] nanowires. The complex shape of the current wires can be explained by an interplay of the relative diffusion rate of the different adatoms on the nanowire surface,[22] which leads to the segregation of the most

slowly diffusing species (in this case Al) at all edges between two facets. Different from other core–shell nanowires reported in the literature, however, is that the complex core–shell structure of our $Al_xIn_{1-x}P$ has not been grown intentionally, but is spontaneously formed during axial growth.

In light of these peculiar results, our reconstruction of the growth history of these WZ $Al_{0.25}In_{0.75}P$ nanowires is as follows: the nanowire is nucleated on the (111)A InP surface, and the core is formed, which starts growing perpendicular to the substrate, along the [0001] direction. The core has {10−12} top facets and slanted side facets which belong to the {30−31} family (see section S3 in the Supporting Information). We speculate that the presence of slanted facets triggers shell growth, which starts from the rim of the top facets of the core (see section S3 in the Supporting Information for further details). Because of different elemental incorporation rates for different facets, core and shell have slightly different composition, as shown in Figure 2a−c. The Al-rich segregations form at the edges between the facets of the nanowire throughout the entire growth, giving rise to the peculiar pattern visible in Figure 2a−c. The segregations are therefore running along the whole length of the nanowire (see section S3 in the Supporting Information).

For determination of the spatial origin of optical emission, a cathodoluminescence (CL) study on a WZ $Al_{0.25}In_{0.75}P$ nanowire (still on its substrate) has been performed at 300 K, by scanning a 5 kV electron beam across its top and simultaneously collecting a spectrum and the secondary

electron intensity. The resulting spatial map for this nanowire is compared to the TEM/EDS results for the lamella in Figure 2a−c (see section S4 in the Supporting Information for methods). The nanowire is raster-scanned using 10 nm steps. A CL spectrum is shown in Figure 2d, collected from an outer region of the nanowire, where we can observe two emission peaks, one at 615 nm (2.05 eV) and one, with lower intensity and broader, around 690 nm (1.8 eV). In Figure 2e,f the integrated CL intensity maps for the two peaks are shown. The integrated intensity of the 615 nm peak, shown in Figure 2e, is higher when exciting the core of the nanowire, while the peak around 690 nm is visible only when exciting at the edges of the nanowire, as shown in Figure 2f, where we observed the In-rich shell in the lamella in Figure 2a−c. Knowing the structure of the nanowires from the TEM/EDS study in Figure 2a−c (and section S3 in the Supporting Information), we conclude that the 615 nm peak is emitted by the core, while the peak around 690 nm is emitted by the shell, with these two regions separated by the Al-rich segregations, which act as a barrier for the carriers due to their higher band gap. The intensity variations observed in Figure 2e when probing the core are likely due to lower excitation efficiency and therefore lower emission from the edges and tip of the nanowire.[24,25]

We now proceed to investigate the photoluminescence properties of WZ $Al_xIn_{1-x}P$ (see section S5 in the Supporting Information for methods). In Figure 3a we show the photoluminescence spectra of WZ $Al_xIn_{1-x}P$ nanowire arrays as a function of the Al fraction ($0 \leq x \leq 0.40$). Importantly, the room-temperature (300 K) emission can be tuned between the near-infrared (875 nm, 1.43 eV) and the green (555 nm, 2.23 eV). The low-temperature (10 K) spectra of the same nanowire arrays are shown in section S5 in the Supporting Information. The spectra are broadened (i.e., full width at half-maximum at 300 K fwhm = 55 meV for WZ InP and fwhm = 120 meV for WZ $Al_{0.25}In_{0.75}P$), likely because of alloy fluctuations. In addition, the WZ $Al_{0.05}In_{0.95}P$ and WZ $Al_{0.15}In_{0.85}P$ nanowires have stacking faults (see section S2 in the Supporting Information) which lead to broadening, as these defects might result in a staggered type II band alignment between the WZ and ZB segments, which in turn cause radiative transitions at lower energy than the band gap.[26,27] A longer wavelength emission is present in various WZ $Al_xIn_{1-x}P$ spectra, because of compositional fluctuations and the presence of portions of the nanowires with lower Al content, as seen in Figure 2. The integrated photoluminescence intensity at 10 and 300 K is shown in Figure 3b as a function of composition. We integrated only the main peak of the nanowires, neglecting the lower-energy tail, as we have previously determined through CL that it is caused by inhomogeneities in the nanowires, for example, an indium-rich shell as shown in Figure 2. At 10 K all samples emit with a similar intensity, within a factor of 5, while possessing the same volume. At 300 K the integrated intensity decreases from WZ InP to $Al_{0.40}In_{0.60}P$ by a factor of 50. The ratio of the integrated PL intensity at 300 and 10 K (I_{300K}/I_{10K}) is presented in Figure 3c. Although this ratio decreases with increasing Al content, all samples have a I_{300K}/I_{10K} ratio within 1 order of magnitude. The decrease of the emission intensity with increasing Al is less than what we expected on the basis of the surface recombination velocities measured in ZB $Al_xIn_{1-x}P$.[28] The surface recombination in $Al_xIn_{1-x}P$ is expected to reduce the photoluminescence emission by 3 orders of magnitude compared to InP because of the shortening of the nonradiative lifetime.[28] Furthermore, Al-containing III/V

semiconductors often suffer from increased bulk recombination losses due to binding of oxygen impurities.[29] An additional cause of nonradiative recombination can be phosphorus (P) vacancies, which are expected to increase with the aluminum fraction, as we used a lower V/III ratio during growth (see section S1 in the Supporting Information).[30] We tentatively explain the strong photoluminescence intensity of WZ $Al_xIn_{1-x}P$ in the yellow−green range by the core−shell structure which is visible in our cross-sectional TEM data. Aluminum-rich segregations forming at the edges of the facets confine the charge carriers in the inner pockets and prevent carrier diffusion to the outermost surface of the nanowire.[31]

For insight on the nature of the optical transitions involved, the WZ $Al_xIn_{1-x}P$ samples are investigated with time-resolved photoluminescence (TRPL). The PL decay curves are fitted with a single exponential, yielding the photoexcited carrier lifetime, as shown in the inset of Figure 3d. The carrier lifetime is reported as a function of composition, at 10 K (circles) and 300 K (triangles). We report two data points for WZ InP, corresponding to the band-gap-related (BGR) and donor−acceptor pair (DAP) transition peaks at 10 K (see section S5 in the Supporting Information).[32] The BGR peak shows a very short lifetime of 0.5 ± 0.1 ns, while the DAP peak shows a 2 orders of magnitude longer lifetime of 80 ± 5 ns. A short lifetime is typical for a direct recombination with high oscillator strength, while the long lifetime of the DAP peak is explained by the small overlap of the carrier wave functions in the impurity pairs, which lowers the recombination rate.[33] For all WZ $Al_xIn_{1-x}P$ compositions a lifetime between 0.5 and 1.5 ns at 10 K is observed, which is comparable to other high-quality direct band gap III/V nanowires emitting through an optical transition with high oscillator strength.[18,34,35] The lifetime at 300 K is substantially lower than at 10 K and is very close to the instrumental resolution lower limit of about 0.3 ns for most WZ $Al_xIn_{1-x}P$ samples. This short lifetime at 300 K is likely due to surface recombination being more effective at room temperature. Using $\frac{1}{\tau} = \frac{1}{\tau_{bulk}} + \frac{4S}{d}$, in which S is the surface recombination velocity, and d is the nanowire diameter, a typical lifetime for an unpassivated InP nanowire grown with SA-MOVPE[35,36] is around 1 ns ($S \approx 2200$ cm/s). The expected lifetime for our unpassivated $Al_xIn_{1-x}P$ nanowires ($S \approx 10^6$ cm/s), based on the experimental value of surface recombination reported in the literature for ZB $Al_xIn_{1-x}P$,[37,38] should only be 1 ps. The relatively long lifetime of the WZ $Al_xIn_{1-x}P$ nanowires is probably due to the confinement of carriers in the inner pockets by the Al-rich shell. The decrease of the lifetime at higher temperature can be explained by carrier detrapping; at higher temperature they might escape and increase the probability of nonradiative recombination at the surface.

For an understanding of the origin of the light emission in WZ $Al_xIn_{1-x}P$, the electronic band structure and the oscillator strength have been calculated as a function of the composition x. The calculations have been performed using total-energy calculations in the framework of the density functional theory with the exchange-correlation functional in local density approximation (LDA)[39] as implemented in the Vienna ab initio simulation package (VASP).[40] To compute the electronic band structure, we consider the nonlocal HSE06 hybrid exchange-correlation functional with the spin−orbit coupling included via noncollinear description. This functional is well-known to give eigenvalues and eigenfunctions close to the quasiparticle excitation.[41−43] The ternary compounds are

modeled by various local atomic arrangements. Thereby, the positions of the substitutional aluminum and indium ions in the cation sublattice determine the band structure.[44,45] We optimize the atomic geometry of the local atomic configurations in 48-atom supercells. The alloy composition is simulated by distributing the Al (In) atoms in four different ways as discussed below. For each resulting atomic geometry we investigate its band structure near the Γ point in the small Brillouin zone of the supercell. The corresponding wave functions are used to compute the squares of the momentum matrix elements between the highest occupied band states and the lowest empty ones.

First, the alloy for a given composition x is simulated by distributing the Al atoms starting (i) from homogeneous alloys on an atomic scale, where substitutional cations occupy positions which are uniformly distributed throughout the sublattice. For such configurations, the lowest optical transitions in the band structure obtained as a function of the composition do not match the experimentally observed peak positions (see section S6 in the Supporting Information). For this (i) distribution a direct to pseudodirect conduction band crossover is predicted around $x = 0.25$, which would make room-temperature emission in the yellow and green range inefficient, contrary to what is experimentally observed. In fact, according to the optical transition selection rules for ideal wurtzite, the only allowed transition (for in-plane light polarization) is the $\Gamma_{7c}-\Gamma_{9v}$, while the $\Gamma_{8c}-\Gamma_{9v}$ is predicted to be forbidden at the Γ point.[41,46] One reason for our finding may be related to the fact that the internal strain due to different Al−P and In−P bond lengths can be better accommodated in nonhomogeneous cation distributions.

Therefore, the band structure for three other disordered cation configurations is calculated, and the results are averaged, to account partially for effects of the configurational entropy and light emission from different atomic arrangements but equal composition (see section S6 in the Supporting Information for details). We simulate (ii) clustered situations, where the Al (In) atoms occupy near positions in the cation sublattice; (iii) completely randomly generated distributions, where the cation positions are chosen randomly before simulation; and (iv) a superlattice arrangement, where the In and Al atoms occupy alternating planes along [0001]. Since we consider all these configurations as likely present in the material at the same time, the results are averaged for these configurations, where we apply equal weights in averaging, assuming that they can be locally realized with the same probability. The averaged theoretical results are compared with the photoluminescence data in Figure 4a, where the lines represent the theoretical calculations, while the circles indicate the energy of the PL emission as a function of the composition. The calculated and experimental data show an excellent quantitative agreement. The oscillator strength of the conduction band minimum−valence band maximum (CBM−VBM) transition is calculated and shown in Figure 4b, as the ratio between Kane energy and band gap energy.[41] The oscillator strength is high for all the compositions studied experimentally, which agrees with our observation of strong photoluminescence at room temperature between the infrared and green range.

In conclusion, we have developed novel WZ $Al_xIn_{1-x}P$ nanowires with aluminum fraction between $0 \leq x \leq 0.40$, with strong optical emission between the near-infrared 875 nm (1.42 eV) and the "pure green" 555 nm (2.23 eV) at room
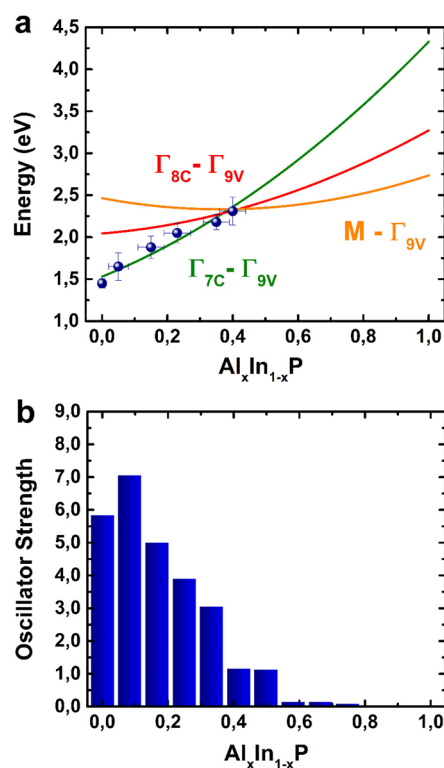

Figure 4. (a) Optical transitions of WZ $Al_xIn_{1-x}P$ in function of the aluminum fraction x. Green (red) [orange] line: calculated energy values of the $\Gamma_{7C}-\Gamma_{9V}$, ($\Gamma_{8C}-\Gamma_{9V}$), and [M-Γ_{9V}] transition. Bulk band denotations are used. Our predictions are obtained by averaging over four different disordered cation configurations. Circles: experimental PL energy. The composition of the samples was determined by EDS as described in the main text. The error bar on the energy values is the fwhm of the PL peak. The quantitative agreement between experimental and theoretical data is excellent. (b) DFT-calculated oscillator strength of the transition between conduction band minimum and valence band maximum in WZ $Al_xIn_{1-x}P$ as a function of the Al fraction x.

temperature, showing relatively high I_{300K}/I_{10K} ratio, with values comparable to WZ InP. We therefore conclude that WZ $Al_xIn_{1-x}P$ nanowires demonstrate strong promise for solid state lighting applications. Future work will be aimed at improving the radiative efficiency in the green range, for instance, by improving the compositional homogeneity and passivating the nanowire surfaces.

■ ASSOCIATED CONTENT

Ⓢ Supporting Information

The Supporting Information is available free of charge on the ACS Publications website at DOI: 10.1021/acs.nanolett.8b00621.

Additional information on growth, crystal structure, analysis methods, and simulations (PDF)

■ AUTHOR INFORMATION

Corresponding Author
*E-mail: l.gagliano@tue.nl.

ORCID Ⓘ
L. Gagliano: 0000-0003-4214-8639
S. Koelling: 0000-0002-6606-9110
J.E.M. Haverkort: 0000-0003-3051-673X

E.P.A.M. Bakkers: 0000-0002-8264-6862

■ **REFERENCES**

(1) Pimputkar, S.; Speck, J. S.; DenBaars, S. P.; Nakamura, S. Prospects for LED lighting. *Nat. Photonics* **2009**, *3*, 180−182.

(2) Pan, C.; et al. High-resolution electroluminescent imaging of pressure distribution using a piezoelectric nanowire LED array. *Nat. Photonics* **2013**, *7*, 752−758.

(3) Ryu, H. Y.; et al. A comparative study of efficiency droop and internal electric field for InGaN blue lighting-emitting diodes on silicon and sapphire substrates. *Sci. Rep.* **2017**, *7*, 44814.

(4) Jeong, H.; et al. Carrier localization in In-rich InGaN/GaN multiple quantum wells for green light-emitting diodes. *Sci. Rep.* **2015**, *5*, 9373.

(5) Khan, A. Semiconductor photonics: Laser diodes go green. *Nat. Photonics* **2009**, *3*, 432−434.

(6) Auf Der Maur, M.; Pecchia, A.; Penazzi, G.; Rodrigues, W.; Di Carlo, A. Efficiency Drop in Green InGaN/GaN Light Emitting Diodes: The Role of Random Alloy Fluctuations. *Phys. Rev. Lett.* **2016**, *116*, 1−5.

(7) Shim, J.-I.; et al. Efficiency droop in AlGaInP and GaInN light-emitting diodes. *Appl. Phys. Lett.* **2012**, *100*, 111106.

(8) Jiang, L.; et al. GaN-based green laser diodes. *J. Semicond.* **2016**, *37*, 111001.

(9) Berg, A.; et al. Radial Nanowire Light-Emitting Diodes in the (AlxGa1-x)yIn1-yP Material System. *Nano Lett.* **2016**, *16*, 656−662.

(10) Li, C.; et al. Nonpolar InGaN/GaN Core-Shell Single Nanowire Lasers. *Nano Lett.* **2017**, *17*, 1049−1055.

(11) Van Dam, D.; et al. Directional and Polarized Emission from Nanowire Arrays. *Nano Lett.* **2015**, *15*, 4557−4563.

(12) Kölper, C.; et al. Core-shell InGaN nanorod light emitting diodes: Electronic and optical device properties. *Phys. Status Solidi A* **2012**, *209*, 2304−2312.

(13) Ishizaka, F.; Hiraya, Y.; Tomioka, K.; Motohisa, J.; Fukui, T. Growth of All-Wurtzite InP/AlInP Core-Multishell Nanowire Array. *Nano Lett.* **2017**, *17*, 1350−1355.

(14) Qian, F.; et al. Multi-quantum-well nanowire heterostructures for wavelength-controlled lasers. *Nat. Mater.* **2008**, *7*, 701−6.

(15) Chu, S.; et al. Electrically pumped waveguide lasing from ZnO nanowires. *Nat. Nanotechnol.* **2011**, *6*, 506−10.

(16) Assali, S.; et al. Direct band gap wurtzite gallium phosphide nanowires. *Nano Lett.* **2013**, *13*, 1559−63.

(17) Gao, Q.; et al. Selective-Area Epitaxy of Pure Wurtzite InP Nanowires: High Quantum Efficiency and Room-Temperature Lasing. *Nano Lett.* **2014**, *14*, 5206.

(18) Gagliano, L.; et al. Pseudodirect to Direct Compositional Crossover in Wurtzite GaP/InxGa1-xP Core-Shell Nanowires. *Nano Lett.* **2016**, *16*, 7930−7936.

(19) Yeh, T. W.; et al. InGaN/GaN multiple quantum wells grown on nonpolar facets of vertical GaN nanorod arrays. *Nano Lett.* **2012**, *12*, 3257−3262.

(20) Hersee, S. D.; Sun, X.; Wang, X. The controlled growth of GaN nanowires. *Nano Lett.* **2006**, *6*, 1808−1811.

(21) Yin, X.; Wang, X. Kinetics-Driven Crystal Facets Evolution at the Tip of Nanowires: A New Implementation of the Ostwald-Lussac Law. *Nano Lett.* **2016**, *16*, 7078−7084.

(22) Sköld, N.; et al. Phase segregation in AllnP shells on GaAs nanowires. *Nano Lett.* **2006**, *6*, 2743−2747.

(23) Heiss, M.; et al. Self-assembled quantum dots in a nanowire system for quantum photonics. *Nat. Mater.* **2013**, *12*, 439−44.

(24) Tchernycheva, M.; et al. Core−shell InGaN/GaN nanowire light emitting diodes analyzed by electron beam induced current microscopy and cathodoluminescence mapping. *Nanoscale* **2015**, *7*, 11692−11701.

(25) Meuret, S. Nanoscale relative emission efficiency mapping using cathodoluminescence g2 imaging. *Nano Lett.* **2018**, *31*, 2288.

(26) Akopian, N.; Patriarche, G.; Liu, L.; Harmand, J.-C.; Zwiller, V. Crystal phase quantum dots. *Nano Lett.* **2010**, *10*, 1198−201.

(27) Assali, S.; et al. Crystal Phase Quantum Well Emission with Digital Control. *Nano Lett.* **2017**, *17*, 6062−6068.

(28) Boroditsky, M.; et al. Surface recombination measurements on III-V candidate materials for nanostructure light-emitting diodes. *J. Appl. Phys.* **2000**, *87*, 3497.

(29) Arehart, A. R.; Brenner, M. R.; Zhang, Z.; Swaminathan, K.; Ringel, S. A. Traps in AlGaInP materials and devices lattice matched to GaAs for multi-junction solar cells. *Conf. Rec. IEEE Photovolt. Spec. Conf.* **2010**, 1999−2001.

(30) Swaminathan, V.; Lopata, J.; Slusky, S. E. G.; Dautremont-Smith, W. C.; Pearton, S. J. Increase in photoluminescence of Zn-doped p-type InP after hydrogenation. *Electron. Lett.* **1989**, *25*, 1584−1586.

(31) Stettner, T. Coaxial GaAs-AlGaAs core-multishell nanowire lasers with epitaxial gain control. *Appl. Phys. Lett.* **2016**, *108*, 011108.

(32) Zilli, A.; et al. Temperature dependence of interband transitions in wurtzite InP nanowires. *ACS Nano* **2015**, *9*, 4277−4287.

(33) Yu, P. Y.; Cardona, M. *Fundamentals of Semiconductors*; Springer: Berlin Heidelberg, 2010; DOI: 10.1007/978-3-642-00710-1.

(34) Signorello, G.; et al. Inducing a direct-to-pseudodirect bandgap transition in wurtzite GaAs nanowires with uniaxial stress. *Nat. Commun.* **2014**, *5*, 3655.

(35) Wang, F.; et al. Spatially resolved doping concentration and nonradiative lifetime profiles in single Si-Doped InP nanowires using photoluminescence mapping. *Nano Lett.* **2015**, *15*, 3017−3023.

(36) Black, L. E.; et al. Effective Surface Passivation of InP Nanowires by Atomic-Layer-Deposited Al2O3 with POx Interlayer. *Nano Lett.* **2017**, *17*, 6287−6294.

(37) Boroditsky, M.; et al. Surface recombination measurements on III-V candidate materials for nanostructure light-emitting diodes. *J. Appl. Phys.* **2000**, *87*, 3497.

(38) Jeng, M. J.; Chang, Y. H.; Chang, L. B.; Huang, M. J.; Lin, J. C. Effective suppression of surface recombination of AlGaInP light-emitting diodes by sulfur passivation. *Japanese J. Appl. Physics, Part 2 Lett.* **2007**, *46*, L291.

(39) Perdew, J. P.; Wang, Y. Accurate and simple analytic representation of the electron-gas correlation energy. *Phys. Rev. B: Condens. Matter Mater. Phys.* **1992**, *45*, 13244−13249.

(40) Kresse, G.; Furthmüller, J. Efficient iterative schemes for ab initio total-energy calculations using a plane-wave basis set. *Phys. Rev. B: Condens. Matter Mater. Phys.* **1996**, *54*, 11169−11186.

(41) Bechstedt, F.; Belabbes, A. Structure, energetics, and electronic states of III-V compound polytypes. *J. Phys.: Condens. Matter* **2013**, *25*, 273201.

(42) Heyd, J.; Scuseria, G. E.; Ernzerhof, M. Hybrid functionals based on a screened Coulomb potential. *J. Chem. Phys.* **2003**, *118*, 8207−8215.

(43) Paier, J. Screened hybrid density functionals applied to solids. *J. Chem. Phys.* **2006**, *124*, 154709.

(44) Christian, T. M.; et al. Amber-green light-emitting diodes using order-disorder AlxIn1−xP heterostructures. *J. Appl. Phys.* **2013**, *114*, 74505.

(45) Zhao, J.; Tang, X.; Teng, J.; Yong, A. M. Atomic ordering of AlInP grown by MOVPE using TBP with different V/III ratios in pure ambient N2. *J. Cryst. Growth* **2010**, *312*, 1505−1509.

(46) De, a.; Pryor, C. E. Predicted band structures of III-V semiconductors in the wurtzite phase. *Phys. Rev. B: Condens. Matter Mater. Phys.* **2010**, *81*, 155210.